Original Article

Analysis Effect On Boron In Grade 40 Cast Iron

Rahul Kumar[1], Pankaj Kumar[1],

1. **Assistant Professor, Subharti Polytechnic College, SVSU**

Abstract

As we know, nowadays use of boron in automotive steels progressively contaminates cast iron charge mixtures. There are opinions about the effect of boron on the structure and the properties of cast iron no agreement about acceptable critical concentrations of this element. Therefore, an experimental study was perform to uncover the effects of boron in gray cast iron of Garde-40. Ferro-boron additions increased boron up to 130 parts per million in laboratory heat. Thermal analysis was utilize to determine the effect of boron on phase transformations during eutectoid transformation and solidification. Mechanical property test and microstructural analysis were conduct to assess the effect of boron on different carbon equivalents. The results showed that the effect of boron in gray cast iron was significantly affected by carbon equivalent. A preliminary discussion about the mechanisms of boron effects on phase transformations and properties of gray cast iron is present

Key words: Boron, Cast Iron, Thermal Analysis

Address for correspondence: Rahul Kumar, Subharti Polytechnic College, Swami Vivekanand Subharti University, Meerut, UP, 250005

Mail: khalsa.pankaj@gmail.com **Contact:** +91- 9927078544

Introduction

Casting capabilities, sound physical and mechanical properties, simplicity in production, and the lost cost makes gray cast iron versatile in industrial applications. Although most properties are affected by the chemical content of elements like C, Si, Mn, and Cr the trace elements in gray cast iron also have their fair part of the contribution towards enhancing the properties of the casting. One of these trace elements which has been causing some problems for the Iron foundries is boron.

During the last decade, the addition of boron to automotive-grade steel has increased. The hardenability provided by boron has found many applications in automotive panel-grade steels. This boron-added steel then finds its way through waste into the gray cast iron charges. Problems have been received from the gray cast iron foundries about intended quality control issues with such boron-added material. Another source of boron in gray cast iron can be the fresh furnace linings.

The effect of boron on gray cast iron is not very precisely studied. Boron is known as a strong carbide stabilizer. According to Ankama et.al [1], the presence of boron above 550ppm can be disastrous to the iron in terms of chill and cracking problems in thin section castings. It can also cause the formation of undesired graphite flake structures like another grade of boron and reduce the strength of the material. Smaller graphite structures like another grade of boron can create small carbon diffusion distances from the matrix to the graphite flakes ultimately creating regions of ferrite that can adversely affect the mechanical properties of gray cast iron. Boron is recommended to be maintained under 50 ppm to avoid the chill.

The effect of boron is that it is a ferrite stabilizer [2]. Presence can cause severe effects on pearlitic grades of gray cast iron. Boron may prevent with pearlite stabilizing elements like Cu and Mn resulting in 'soft' pearlitic castings. Prevents the diffusion of carbon and Cu alloying tend to segregate to the austenite-graphite interfaces, resulting in the transformation of austenite into pearlite. Therefore, disrupting the effect of Cu and boron may accumulate around graphite. This segregation of boron was confirmed by another author using secondary ion mass spectroscopy [3]. Boron was detected surrounding graphite nodules in ductile iron. The boron content used in that study was 50 to 60 ppm. The ferrite stabilizing effect of boron was also shown in ductile iron [4] where specimens higher in boron were found to have an increased amount of free ferrite and consequently a reduction in pearlite.

The effect of boron on austenite is said to be similar to that of Ti, and boron additions can stabilize nitrides that serve as substrates for the nucleation of austenite [5]. Another effect can be increased undercooling and the reduction of graphite nucleation potential. The effect of boron on graphite flake size was studied by Alexander et.al [6]. The study concluded that the higher additions of boron reduce graphite flake size. Therefore, it should be noted that this study dealt with B levels of 0.003wt. % to as high as 0.34wt. %. In the same study, increasing boron content was seen to decrease the temperature gap between liquidus and solidus temperatures and increase the undercooling effects.

The purpose of this check, funded by the American Foundry Society, is to provide experimental information on the effects of boron in gray cast iron of different grades. This article reports Phase-I results dedicated to Class-40 cast iron. The properties under investigation were thermal analysis parameters, microstructure, chilling tendency, strength, and hardness.

Methodology

Two types of Grade 400 GI heat was cast in the laboratory. Heats were perform in a 210lbs induction furnace. The first heat was plan to be a high carbon equivalent (CE) heat with a CE target of 4.3-4.4 (high-CE) the second with a CE target of 4.0-4.1 (medium-CE). Future studies will be perform with low CE also (3.8-3.9) effect of boron was study across four different levels of boron addition for the same chemistry. The initial chemistry had no boron addition. Then the boron was intentionally added in level of 20ppm, 40ppm, and 100ppm. The boron addition was complete in the induction furnace to enhance the boron recovery [6].

The charge for both the heat consist of high-purity induction iron ingots, ferrosilicon, ferromanganese, metallic chromium, high-purity graphite, and foundry returns from our foundry sponsor (Table 1). An argon cover at a flow rate of 25 SCFH was use to increase recovery rates. The target chemistries for high-CE and medium-CE heats are given in the Table.2

* Inoculant composition: Si: 70wt. %; Al: 0.17wt. %; Sr: 0.76wt. %; Co: 0.039wt. %

Table 1. Chemical composition (wt. %)
Si target before inoculation

Heat	C	Si	CE	B (ppm)	Cr	Mn
High-CE heat	3.40	2.5 - 2.6	4.3	2/20/40/100	0.10 - 0.15	0.20 – 0.30
Medium-CE heat	3.35	1.8 - 1.9 #	4.0	2/20/40/100	0.15 - 0.20	0.45 – 0.55

Check the CE in the melt, thermal analysis with tellurium (Te) added cups were used. The tapping temperature for the heat was maintained between 1360-1380°C. The metal was tapped into 22lbs hand ladles. A total of four chemistries were planned for the heats with varying boron additions. The 1st chemistry was no boron-added, 2nd 20ppm. 3rd 40ppm and the 4th 100ppm boron additions. Chemistry required two hand ladles. The inoculation was done for each hand ladle during tapping. The inoculant used for the heats was Superseded (Si 70%) and was taken as 0.2% weight of each hand ladle capacity.

In order to check the chemical composition of each chemistry, two types of samples were taken: an immersion sample and a sample poured into a Cu chill mold. To understand the boron effect on the mechanical properties of gray cast iron, multiple molds were poured for each chemistry, including a step block, ASTM A48 B-bar molds, and a chill wedge. The step block (Figure 1) had four steps 5, 10, 20, and 30mm. A total of 6 boron-bar samples were obtained from each chemistry.

Charge Source	C	Si	B	Cr	Mn	Cu	P	S
Waupaca foundry returns	3.46	2.14	0.0004	0.21	0.58	0.21	0.029	0.086
Induction iron	0.0017	0.002	0.0001	0.01	0.01	0.002	0.005	0.0025
Ferro-Silicon (Fe75Si)	--	75	--	--	--	--	--	--
Ferro-B (Fe18B)	0.26	0.57	18.52	--	--	--	0.028	0.003
Desulco graphite	99.99	--	--	--	--	--	--	--
Inoculant *	--	70	--	--	--	--	--	--
Metallic chrome	-	-	--	98	--	--	--	--
Ferro-Manganese	1.00	1.00	--	--	76	--	--	--

Table 2. Target chemistries (wt. %) for the heats.

Perform thermal analysis by obtaining the cooling curves from ATAS software using non-Te-coated cups. The obtained cooling curves were used to analyze the effects of boron on eutectic and eutectoid reactions. The variation in critical parameters of the cooling curves was studied as suggested in the work of J. Sertucha et.al [7] and Stefanescu et.al [8] to understand the effect of boron on solidification and solid-state transformations of gray iron. The nomenclature of the used parameters is shown in Figure 2[8].

Step blocks taken in specimens for optical metallography. The specimens were sectioned from the center of the step block and the center of each step as shown in (Figure1). Polishing for optical metallography was performed by standard metallographic techniques. Unetched and etched images were taken from each specimen. 3% Nital was used as the etchant. For quantifying the matrix and graphite flake structure, images were analyzed using ImageJ software.

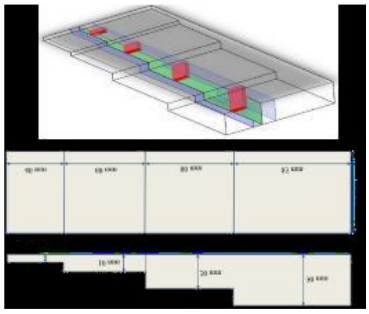

Fig -1: Side, top, and isometric view of step block. The red area was used for metallographic analysis and hardness was measured in the green section.

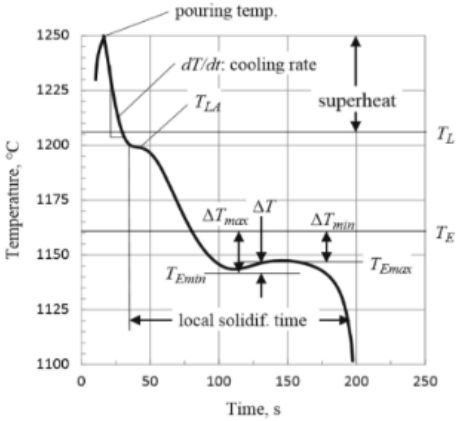

Fig -2: Nomenclature of the used parameters of thermal analysis (from the ATAS software [8].

The chemical composition analysis was done using optical emission arc spectroscopy (OES) and combustion analysis using a commercial C/S and O/N analyzer. The B content of the standards used is given in Table. 3.

Tensile tests were performed on a 250kN servo-hydraulic load frame in accordance with the ASTM A-48[9]. Test bar specifications used for the tensile test were according to the boron-type test bar. The tensile test was performed at a strain rate of 0.02mm/s. Hardness tests were performed on a Brinell hardness tester, and the tests were performed following the ASTM E10-18[10]. Standard hardness blocks were tested before and after the test of actual specimens. Hardness tests were repeated four times per sample and only for the 20mm and 30mm steps of the step blocks.

Table 3. OES calibration for B (ppm). OES values are the average of six measurements.

Standard Name	Certified B (ppm)	OES B (ppm)
BS 4C	2	1
34A	76	72
RN 14/39	30	38
RG 14/161	400	400

The chemical compositions of the heat obtained from the OES are given in Table. 3. To check the boron content as low as possible, a 2ppm boron standard was used. All the standards were tested before testing the actual specimens. The actual chemistries of the heat were close to the target chemistry. It should be noted that Cr and Mn content ranged from 0.12wt.% to 0.20wt.% and 0.30 wt.% to 0.50wt.%, respectively. Si was reduced from 2.7 wt.% to 2.0 wt.% from the high-CE heat to medium-CE heat. The target carbon content was higher for both the heats by 0.1wt.%. In this article, boron additions were used for data analysis.

Table 4: Future comparisons will be performed for heats with different CE using actual boron concentrations.

Heat	Ladle	B-added	C*	Si	CE	B (ppm)	Cr	Mn	Cu	P	S*	Sn	Heat
High-CE Heat	1A	NoB-added	3.56	2.70	4.46	22	0.12	0.29	0.14	0.028	0.064	0.013	1A
	1B	20	3.52	2.77	4.44	38	0.12	0.29	0.13	0.028	0.071	0.013	1B
	1C	40	3.47	2.69	4.37	56	0.12	0.29	0.13	0.028	0.071	0.014	1C
	1D	100	3.53	2.67	4.42	113	0.12	0.29	0.14	0.030	0.074	0.014	1D
Medium-CE Heat	2A	NoB-added	3.45	2.05	4.13	5	0.21	0.58	0.034	0.025	0.020	0.009	2A
	2B	20	3.44	2.07	4.13	25	0.21	0.58	0.036	0.023	0.019	0.008	2B
	2C	40	3.41	2.03	4.09	46	0.21	0.58	0.034	0.024	0.017	0.008	2C
	2D	100	3.39	2.07	4.08	98	0.21	0.59	0.035	0.024	0.018	0.008	2D

* C, and S readings taken from commercial C, S, N, O analyzer

ATAS software obtained for thermal analysis parameters using the non-Te cup is shown in Table. 5. It can be clearly seen from the data that the liquidus temperature
22
(TL) rises as B content increases. This is true for both the heats irrespective of the CE. Another effect that can be noted is that the eutectic minimum temperature (Temin) dropped as the B content increased. The eutectic cooling curves for high-CE heat are shown in Figure 3 and the cooling curve for medium-CE heat is shown in Figure 4. The observations from Table. 5 are clearly visible in these graphs.

Table 5. Thermal analysis data obtained from ATAS software for both the heats.

Heat	High-CE Heat				Medium-CE Heat			
Chemistry	No B-added	20ppm B-added	40ppm B-added	100ppm B-added	No B-added	20ppm B-added	40ppm B-added	100ppm B-added
Liquidus Temp, TL (˚C)	1157.3	1157.3	1158.4	1159.3	1193.3	1195.8	1199.3	1202.2
Eutectic Start (˚C)	1154.9	1154.5	1155.5	1155.1	1176.9	1178.6	1180.3	1180.9
Eutectic Minimum, Temin (˚C)	1151.4	1149.7	1151.4	1150.3	1147.5	1146.3	1146.7	1144.8
Eutectic Maximum, TEmax (˚C)	1154.2	1153.2	1154.8	1153.8	1150.5	1150.1	1149.9	1148.2
Solidus Temp, TSol (˚C)	1109.4	-	1108	1108.4	1100.8	1108.5	1106	1107
Recalescence, ΔT (˚C)	2.8	3.5	3.4	3.5	3.0	3.8	3.2	3.4
Graphite Factor 1	70	-	69	75	72	75	62	71
Graphite Factor 2	20	-	20	17	24	19	32	35

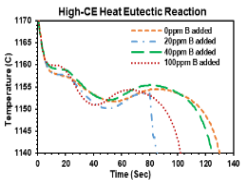

Fig 3. Eutectic cooling curve for high-CE heat.

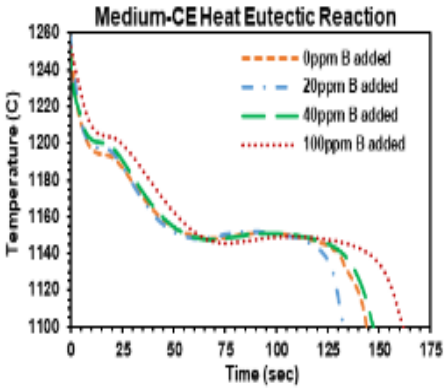

Fig 4. Eutectic cooling curve for medium-CE heat.

The cooling curves shown in Figure 5 and Figure 6 represent the eutectoid reactions for high-CE and medium-CE heats respectively. The red-dotted line represents the VTrans for the eutectoid reactions. Eutectoid parameters like temperatures of eutectoid low and the eutectoid recalescence were analyzed to understand the effect of B in solid-state transformation reactions. In addition, the 1st derivative of the cooling curve was plotted against the temperature for the eutectic and eutectoid reactions to analyze the change in cooling rates related to the latent heat liberation and the eutectoid parameters like VTrans. These graphs are presented in the discussion part of this article.

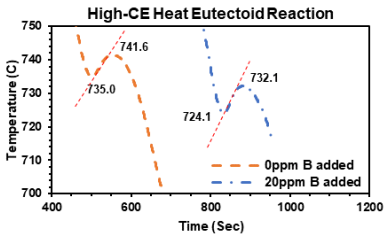

Fig 5. Eutectoid reaction curve for high-CE heat.

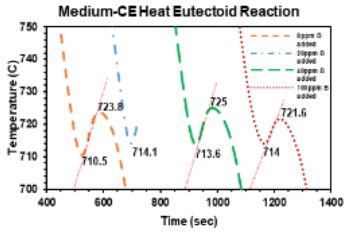

Fig 6. Eutectoid reaction curve for medium-CE heat.

Etched and unetched microstructures obtained from the 30mm step of high-CE heat are shown in Figure 7 and Figure 8. Higher ferrite content is observed in the matrix of higher boron specimens. Although image 1A in Figure 7 seems to have a higher ferrite content, it must be noted that the area represented in the metallographic analysis is very limited and thus cannot be accurately considered as a complete representation of the structure. The unetched and etched microstructures from the 30mm step of the medium-CE heat are shown in Figure 9 and Figure 10. No considerable difference between the specimens can be seen. Although it can be noticed that the ferrite content is higher in high-CE heat as compared to medium-CE heat which is understood because of the higher Si

content in the former. Analysis of the microstructure images from the smaller steps i.e., 10mm and 20mm of both the heats was also performed. As the cooling rates in the smaller steps are higher, the microstructure was mainly pearlite, and the ferrite content of the microstructure was low as compared to the 30mm step. The etched images from the 20mm step for the high-CE and medium-CE are given in Figure 11 and Figure 12, respectively. Similarly, microstructure images from the 10mm step for the high-CE and medium-CE are shown in Figure 13 and Figure 14, respectively.
25
The chill wedge images from high-CE and medium-CE heat are shown in Figure 15 and Figure 16, respectively. The microstructure analysis of the chill wedge was done in five areas, the tip and then at 5mm increments up to 20mm from the tip. It is clearly shown that the chill depth increases for higher boron content for both the heats. The chill depth increased from 7.28mm to 13.1mm as the boron content increased. Carbide structures are visible further away from the tip in higher boron content for both of the heats. Carbide structures in high-CE heat are only seen in the microstructural analysis. The carbide can be seen at a distance of 5mm in the higher boron sample, whereas the low boron samples do not have carbide structures beyond the chill tip portion. This is a clear indicator that boronacts as a carbide stabilizer.

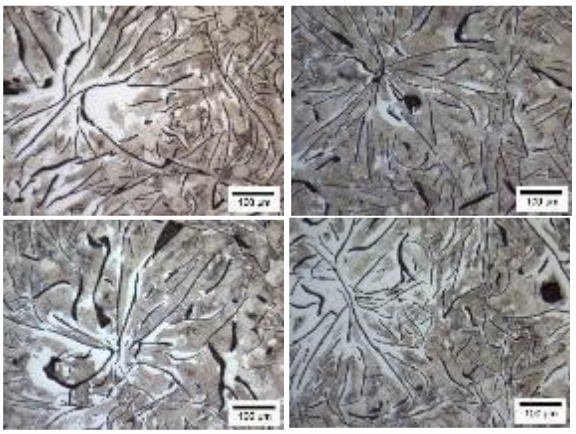

Fig 7. Etched microstructures taken from the 30mm step of the high-CE heat: 1A - no boron-added, 1B - 20 ppm, 1C - 40 ppm, and 1D - 100 ppm boron-added.

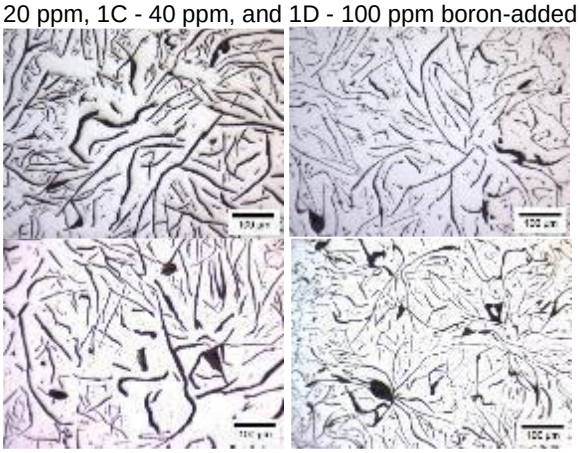

``. Unetched microstructures taken from the 30mm step of the high-CE heat: 1A - no boron-added, 1B - 20 ppm, 1C - 40 ppm, and 1D - 100 ppm boron-added.

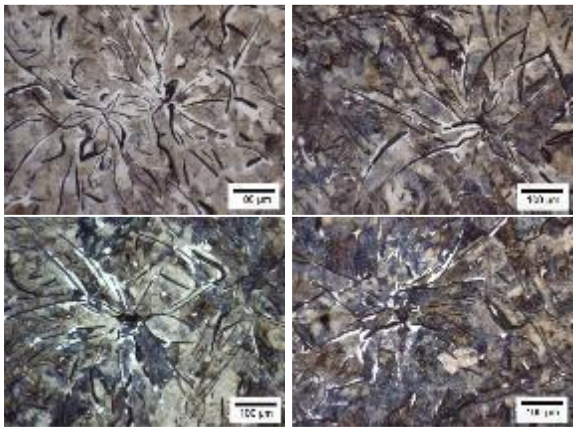

Fig 9. Etched microstructures taken from the 30mm step of the medium-CE heat: 2A - no boron-added, 2B - 20 ppm, 2C - 40 ppm, and 2D - 100 ppm boron-added.

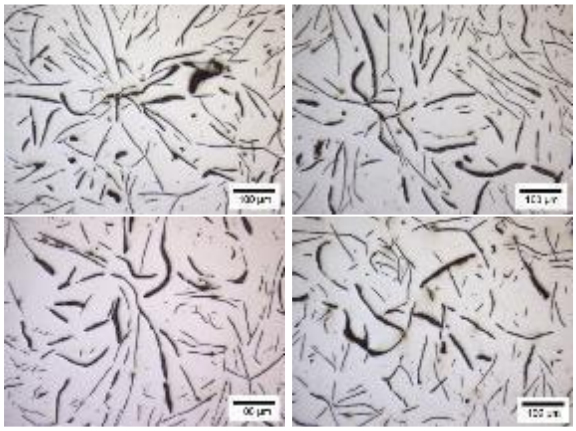

Fig 10. Unetched microstructures taken from the 30mm step of the medium-CE heat: 2A - no boron-added, 2B - 20 ppm, 2C - 40 ppm, and 2D - 100 ppm boron-added.

Fig 11. Etched microstructures taken from the 20mm step of the high-CE heat: 1A - no boron-added, 1B - 20 ppm, 1C - 40 ppm, and 1D - 100 ppm boron-added.

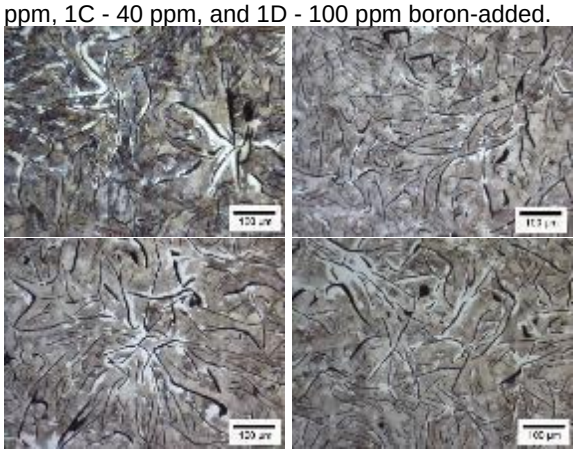

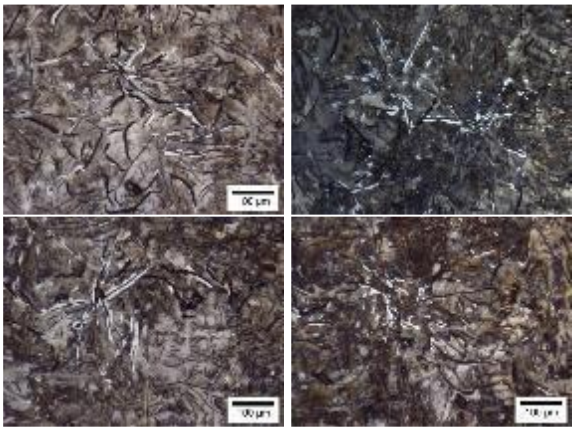

Fig 12. Etched microstructures taken from the 20mm step of the medium-CE heat: 2A - no boron-added, 2B - 20 ppm, 2C - 40 ppm, and 2D - 100 ppm boron-added.

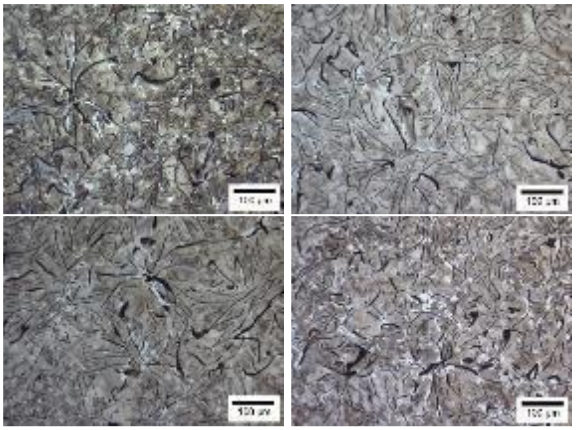

Fig 13. Etched microstructures taken from the 10mm step of the high-CE heat: 1A - no boron-added, 1B - 20 ppm, 1C - 40 ppm, and 1D - 100 ppm boron-added.

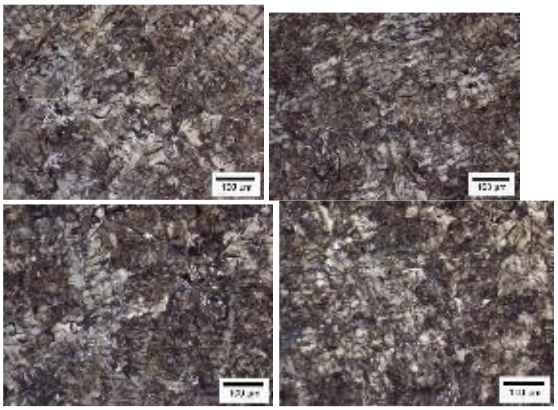

Fig 14. Etched microstructures taken from the 10mm step of the medium-CE heat: 2A - no boron-added, 2B - 20 ppm, 2C - 40 ppm, and 2D - 100 ppm boron-added.

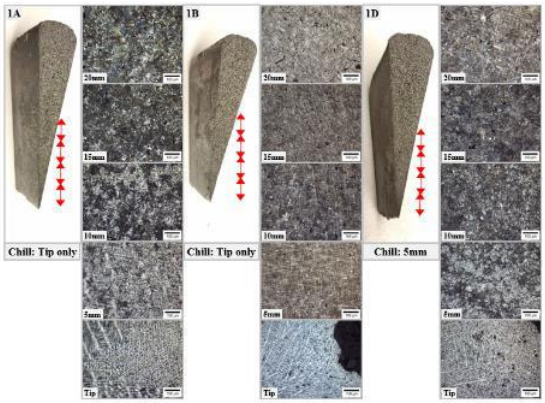

Fig 15. High-CE heat chill wedge fractures and etched microstructures taken at the chill tip and regions at 5mm increments up to 20mm: 1A - no boron-added, 1B - 20 ppm, and 1D - 100 ppm boron-added. The chill tip is not visible in the images.

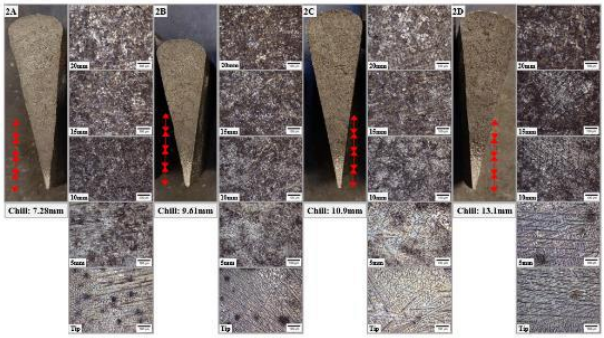

Fig 16. Medium-CE heat chill wedge fractures and etched microstructures taken at the chill tip and regions at 5mm increments up to 20mm: 2A - no B-added, 2B - 20 ppm, 2C - 40 ppm, and 2D - 100 ppm B-added. The chill tip is visible in the images.

The tensile results from the heats are given in Table. 6. The ultimate tensile strength (UTS) of high-CE heat is lower than that of medium-CE heat and this is due to the high levels of Si. A clear trend of increasing tensile strength of the specimens is shown for the medium-CE heat, but this is not the case for high-CE heat. In this heat, the UTS rises for the initial B addition and then decreases when B additions increase. The hardness results are shown in Table. 7 and were in affirmation with the tensile results. The hardness values for the high high-CE heat are lower.

Table 6. Ultimate tensile strengths as a function of boron for both heats.

Heat	Step	No B-added	20ppm B-added	40ppm B-added	100ppm B-added
High-CE heat (CE = 4.43)	Step 4 (30mm)	125± 1	135 ± 5	126 ± 2	125 ± 3
	Step 3 (20mm)	125 ± 5	137 ± 6	128 ± 5	133 ± 2
Medium-CE heat (CE = 4.1)	Step 4 (30mm)	143 ± 2	148 ± 3	153 ± 4	162 ± 3
	Step 3 (20mm)	150 ± 2	153 ± 1	155 ± 5	166 ± 3

Discussion

Two cast irons with high and medium levels of CE were produced with different levels of boron. This study intends to evaluate the specific effect of Boron additions on phase transformations, microstructure, and mechanical properties of gray iron at different CE levels.

3.1. SOLIDIFICATION

Table 7. Hardness (BHN) results as a function of boron for both the heat.

Heat	B-added, ppm	Test 1	Test 2	Test 3	Test 4	Test 5	Test 6	Average TS	Std Dev
High-CE heat (CE = 4.43)	No B-added	20.2	21.0	20.7	20.9	20.6	20.3	20.6	0.32
	20	22.9	23.3	22.4	22.9	22.4	22.8	22.8	0.33
	40	22.4	22.8	21.7	21.2	22.0	22.3	22.1	0.58
	100	20.4	21.6	21.4	20.4	21.8	21.1	21.1	0.60
Medium-CE heat (CE = 4.1)	No B-added	30.6	30.6	27.2	28.5	28.5	28.1	28.9	1.4
	20	32.6	33	28.8	30.3	29.2	28.8	30.5	1.9
	40	33.5	32.7	30	29.8	29.3	29.4	30.8	1.8
	100	33.8	34.9	30.6	30.9	31.3	30.9	32.1	1.8

Both cast irons were hypoeutectic, and solidification started with primary austenite. The cooling curves from both the heats (Figure 3 and Figure 4) show a clearly indicated trend of increasing liquidus temperature with boron additions, which relates to the stimulation of austenite solidification. The effect of boron addition on the eutectic transformation depended on CE. It is known that the undercooling of the eutectic reaction is related to the nucleation of graphite and higher boron content makes it slightly difficult for graphite nucleation and stabilizes austenite. Plots of the 1st derivative of the cooling curve as a function of temperature in Figure 17 and Figure 18 show that the rightmost peak in the plot marks the austenite liquidus temperature. The loop in the graph is the eutectic decalescence. The leftmost point of the loop is the eutectic low temperature, TEmin, while the rightmost point of the loop is the eutectic high, TEmax. The diameter of the loop will give the eutectic decalescence. It is visible that the temperature difference between the austenite liquidus and the eutectic low rises with B content. This trend is observed in both the heats (Figure 17 and Figure 18). The difference between TL and TEmin is shown in Table. 8.)

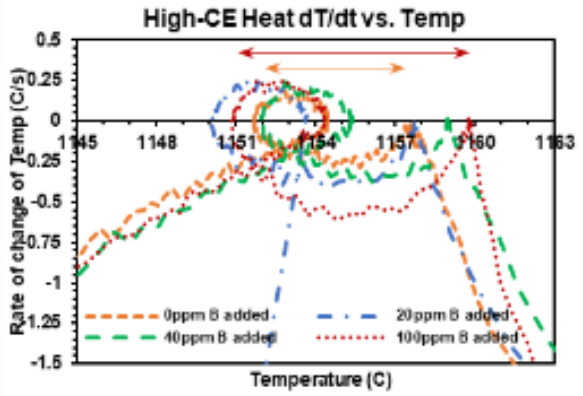

Fig 17. 1st derivative of the cooling curve plotted against temperature for high-CE heat for the solidification. The difference between the TL and TEmin is highlighted by arrows.

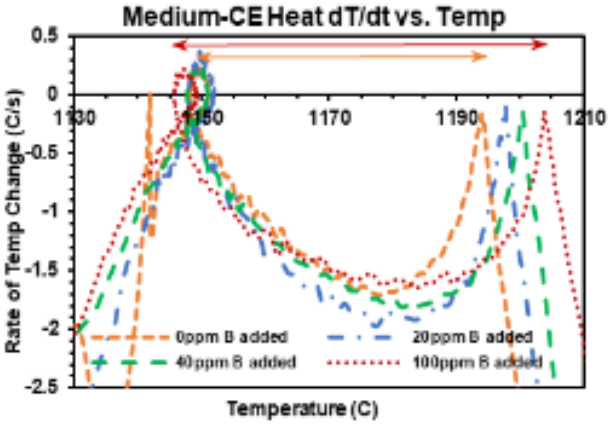

Fig 18. 1st derivative of the cooling curve plotted against temperature for medium-CE heat for the solidification. The difference between TL and TEmin is highlighted by arrows.

Table 8. The difference between the liquidus and eutectic minimum temperature for both the heats.

Heat	B-added, ppm	TL (˚C)	TEmin (˚C)	TL – TEmin
High-CE heat	No B-added	1157.3	1151.4	5.9
	20	1157.3	1149.7	7.6
	40	1158.4	1151.4	7
	100	1159.3	1150.3	9
Medium-CE heat	No B-added	1193.3	1147.5	45.8
	20	1195.8	1146.3	49.5
	40	1199.3	1146.7	52.6
	100	1202.2	1144.8	57.4

Observation and ImageJ quantitative analysis of the unetched microstructures for both heats were done to understand the boron effect on graphite morphology (Figure 19). A measurement error of ±10% is considered for both the heats.

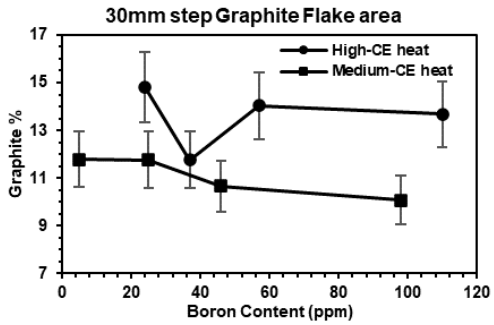

Fig 19. The area of graphite flakes for the 30mm step of the step block for both the heats.

3.2. EUTECTOID TRANSFORMATION

The first derivative of the cooling curve as a function of temperature for high-CE and medium-CE heats are shown in Figure 20 and Figure 21, respectively. Similar to the eutectic graph, the diameter of the loop is the eutectoid decalescence. The parameters VTrans and TTrans are obtained from these curves. The highest value of the first derivative of the cooling curve is called the velocity of transformation (VTrans) whereas the temperature corresponding to this value is TTrans. This data is tabulated in Table 9. In a previous work by Sertucha et.al [7], these parameters were used to predict the ferrite-pearlite formation. When ferrite content in the matrix decreases, and consequently the pearlite content increases, the solid-state transformations occur at lower temperatures and higher Vtrans.

Hence, the eutectoid decalescence is higher during pearlite formation and lower for ferrite formation. In Table. 9 it is seen that both conditions are preferable for ferrite formations for the medium-CE heat with boron additions above 20ppm. However, 20 ppm boron addition increased the VTrans in both heats, which is an indicator that small boron additions can 33 affect the pearlite transformation. These results indicate that the effect of boron on eutectoid reaction is not linear and depended on CE.

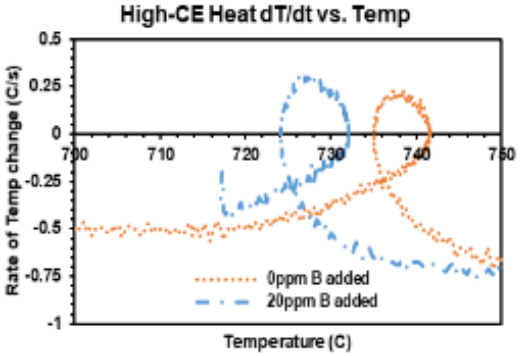

Fig 20. 1st derivative of the cooling curve plotted against temperature for high-CE heat for the eutectoid reaction.

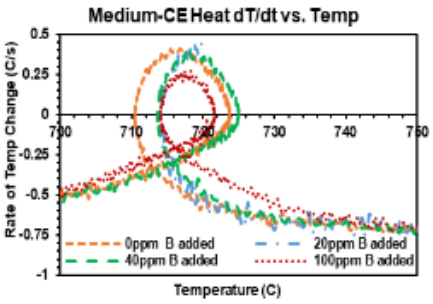

Fig 21. 1st derivative of the cooling curve plotted against temperature for medium-CE heat for the eutectoid reaction.

Table 9. Eutectoid parameters obtained from the cooling curve and the first derivative of the cooling curve of the eutectoid reaction.

Heat	B-added, ppm	Eutectoid Low (˚C)	VTrans, C/s	TTrans (˚C)
High-CE heat	No B-added	735	0.232	738.5
	20	724.1	0.315	726.4
	40	-	-	-
	100	-	-	-
Medium-CE heat	No B-added	710.5	0.411	716.8
	20	714.1	0.442	-
	40	713.6	0.386	717.7
	100	714	0.273	718.3

3.3. MICROSTRUCTURE ANALYSIS

The microstructural analysis of the specimens was used to validate the results obtained from the thermal analysis. The chill wedge analysis was done in order to understand the effect of boron on carbide forming tendency. Images taken from the chill wedges of the high-CE and medium-CE heat are given in Figure 15 and Figure 16, respectively. For the high-CE heat, the chill tip was not visible to the naked eye, whereas, in the case of medium-CE heat, the chill tip was clearly visible. The chill depth for medium-CE heat increased with boron additions. The chill depth measured is shown in the image. To check the carbide structures in high-CE heat, etched microstructures were taken at 5 areas, at the chill tip, and then at 5mm increments from the tip up to a distance of 20mm. The images were then arranged in a way to get a panoramic view of the chill wedge as seen in Figure 15. The same procedure was done for the medium-CE heat as well in Figure 16. As boron increased in high-CE chill samples, carbide became visible in the chill tip. For the highest boron samples, the carbides are seen up to 10mm from the chill tip. For the medium-CE specimens, the carbide precipitates are clearly visible and are seen further away from the chill tip as the amount of boron increases. Analysis of the smallest step, i.e., the 5mm step of the step block, was done as a supplement to the chill wedge analysis. The etched microstructures of the 5mm step are given in Figure 22 and Figure 23 for high-CE and medium-CE heats, respectively. It is clearly shown that there is carbide precipitation in the highest boron sample of the medium-CE heat. The appearance of carbide is a clear indicator of the carbide stabilizing capabilities of boron. The carbide promoting effect of boron may be dependent on the cast iron CE because, at the same

boron level, no such carbide precipitation was shown in the high-CE heat.

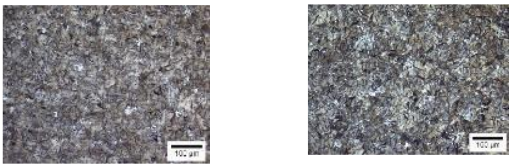

Fig 22. Etched microstructures of the 5mm step of high-CE heat step block, (a) 20ppm B-added and (b) 100ppm B-added. There is no visible carbide precipitation.

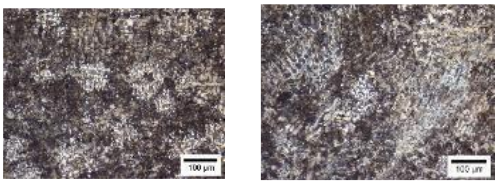

Fig 23. Etched microstructures of the 5mm step of medium-CE heat step block, (a) 20ppm B-added and (b) 100ppm B-added. Carbide precipitation is visible in the highest B sample highlighted by a dashed circle.

The microstructures obtained from the 30mm step of the step block were used to evaluate ferrite forming tendency. In the high-CE heat (Figure 7) the microstructure of the matrix mainly consists of pearlite along with a considerable amount of ferrite enveloping the graphite for all B additions. These specimens had higher amounts of ferrite because of the well-known ferrite stabilizing effect of Si. The microstructures from the 30mm step of the step block of the medium-CE heat are had a mainly pearlitic matrix, with very minor areas of ferrite surrounding the graphite (Figure 9). Using ImageJ for quantification of the ferrite area of images in Figure 7 and Figure 9, the graph in Figure 24 was generated. From the graph, it is shown that the ferrite content for high-CE heat increases with the exception of the specimen without boron (Image 1A in Figure 7). The same effect can be observed for the medium-CE heat, however, the increase in ferrite is very low as compared to high-CE heat. This trend is also observed in the 20mm step as well as the 10mm step. The change in the intensity of the effect of B addition is notable. This effect is more profound in the high-CE heat than that in the medium-CE heat. This is additional proof that the B effect is dependent on CE.

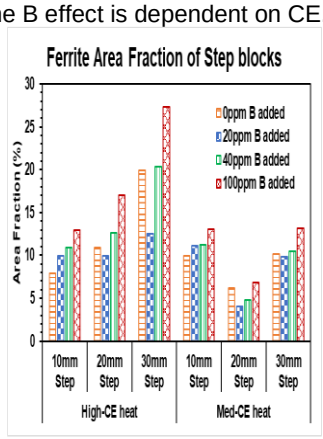

Fig 24. The ferrite area coverage as measured by optical metallography of the step block casting for medium and high CE heats.

3.4. MECHANICAL PROPERTIES

The tensile data are given in Table. 6 for both the heats. In the high-CE heat, the tensile strength increases for the 20 ppm boron addition, but then it tends to reduce for higher boron additions. In the medium-CE heat, a clear trend of increasing UTS with increasing boron content (Figure 25) is observed. A one-way ANOVA analysis and Fisher's Criterion analysis were used for statistical evaluation of these differences at an 80% confidence level. The Fisher analysis graphs are plotted for high-CE heat in Figure 26. Similarly, Fisher analysis graphs are plotted for the medium-CE heat in Figure 28. Based on the results from the statistical analysis, the data is statistically significant with 80% confidence with few exceptions. The hardness specimens were taken from the step block in the area closest to the central plane of the casting (Figure1). The data for both the heats is given in Table. 7. Hardness increased with tensile strength.

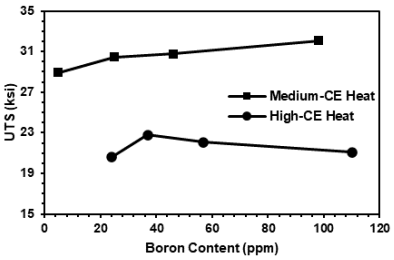

Fig 25. Comparison of UTS as a function of boron for both CE heats.

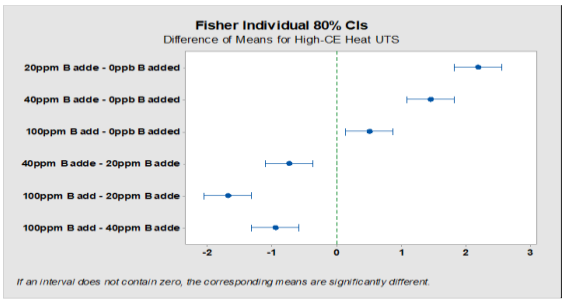

Fig 26. Fisher's analysis of UTS statistical significance as a function of boron for high-CE heat. The top three pairs of test results are significantly different at an 80% confidential level.

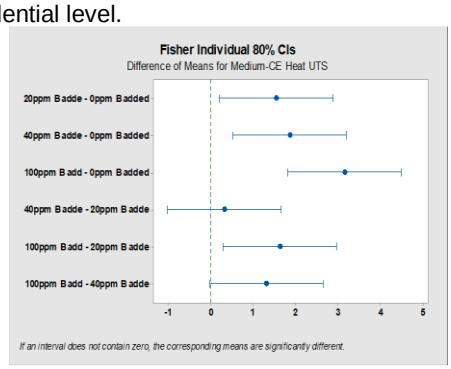

Fig 28. Fisher's analysis of UTS for medium-CE heat as a function of boron content. The results show that UTS is significantly different at an 80% confidence level, except for pairs of 40-20 boron ppm and 100-40 B ppm.

Conclusion

The effects of boron on the microstructure and mechanical properties of gray iron were studied in two heats with high and medium carbon equivalents, CE, related to ASTM A48 Class 30B cast irons. Thermal analysis of the solidification and solid-state cooling curves showed that boron acts as an austenite stabilizer and affects the nucleation of graphite by changing undercooling during the eutectic reaction. The carbide forming tendency of large boron additions was confirmed by a metallographic study of chill wedge depth and step block castings. During the eutectoid reaction, the thermal analysis showed that the effect of boron on the ferrite/pearlite transformation is significant. Boron acts as a ferrite stabilizer when present in high amounts (above 35ppm). However, the effect of low boron additions (less than 20 ppm) was not understood clearly. The microstructural analysis of the heats replicated the results predicted from the thermal analysis, although the intensity of the effect was different for both the heats, suggesting the effect of boron is dependent on CE. More studies will be performed in the future to uncover the mechanisms for the ferrite stabilizing effect of boron. The effect of boron on the mechanical properties of gray iron might also be influenced by the CE of cast iron. In the high-CE heat, tensile strength increased only with 20 ppm boron addition, however, boron additions increased the tensile strength consistently in the medium CE heat. Future work will include a study of boron addition in low CE cast iron, class 30.

Source of Support: Nil
Conflict of interest: Nil
Acknowledgement: None

References

1. Elimination and Neutralization of B in Ductile Irons by. R. L. Naro – ASI International, Ltd., Cleveland, Ohio. J. F. Wallace and Yulong Zhu – Case Western.
2. Doru Michael Stefanescu, Ramon Suarez and Sung Bin Kim, “90 years of thermal analysis as a control tool in the melting of cast iron”, Special review, Vol 17, No 2, (2020).
3. ASTM International. A48/A48M-03(2016) Standard Specification for Gray Iron Castings. West Conshohocken,PA;ASTMInternational,2016.DOI:https://doiorg.libproxy.mst.edu/10.1520/A0048_A0048M-03R16.
4. Alexander I Krynitsky, Harry Stern “Effect of B in structure and Some Physical Properties of Plain Cast Iron”, Research of National Bureau of Standards, Vol 42 (1949).
5. Robert Voigt, “Trace (Minor) Elements in Cast Irons”, ASM Handbook, Volume 1A, Cast Iron Science and Technology (2017).
6. ASTM International. E10-18 Standard Test Method for Brinell Hardness of Metallic Materials. WestConshohocken,PA;ASTInternational,2018.DOI:https://doiorg.libproxy.mst.edu/10.1520/E0010-18.
7. Singh, L.B. (2009). Improvement in properties of grey iron after boron additions. In 57th IFC 2009, 13-15 February 2009 (pp. 166-171). Kolkata, India.
8. Ankamma, K.J.(2014). Effect of Trace Elements (Boron and Lead) on the Properties of Gray Cast Iron. Journal of the Institutions of Engineers. 95 (1), 19-26. DOI: 10.1007/40033-013-031-3.
9. J. Sertucha, R. Suarez, J. Izaga, L. A. Hurtado & J. Legazpi (2006) Prediction of solid-state structure based on eutectic and eutectoid transformation parameters in spheroidal graphite irons, International Journal of Cast Metals Research, 19:6, 315-322, DOI: 10.1179/136404606X167114.
10. Doru M. Stefanescu, “Trace (Minor) Elements in Cast Irons”, ASM Handbook, Volume 1A, Cast Iron Science and Technology (2017).

How to cite this article: Kumar R, Kumar P. Analysis Effect On Boron In Grade 40 Cast Iron Subharti J of Interdisciplinary Research, Dec. 2022; Vol. 5: Issue 3, 24-33